

Detection of mouse liver cancer via a parallel iterative shrinkage method in hybrid optical/microcomputed tomography imaging

Ping Wu
Kai Liu
Qian Zhang
Zhenwen Xue
Yongbao Li
Nannan Ning
Xin Yang
Xingde Li
Jie Tian

Detection of mouse liver cancer via a parallel iterative shrinkage method in hybrid optical/microcomputed tomography imaging

Ping Wu,^a Kai Liu,^b Qian Zhang,^c Zhenwen Xue,^a Yongbao Li,^a Nannan Ning,^d Xin Yang,^a Xingde Li,^e and Jie Tian^a

^aChinese Academy of Sciences, Institute of Automation, Intelligent Medical Research Center, Beijing 100190, China

^bIBM China Research Lab, Building 19 ZGC, Software Park, Beijing 100193, China

^cXidian University, School of Life Sciences and Technology, Xi'an, Shaanxi 710071, China

^dHarbin University of Science and Technology, School of Automation, Harbin, Heilongjiang 150080, China

^eJohns Hopkins University, Department of Biomedical Engineering, Baltimore, Maryland 21205

Abstract. Liver cancer is one of the most common malignant tumors worldwide. In order to enable the noninvasive detection of small liver tumors in mice, we present a parallel iterative shrinkage (PIS) algorithm for dual-modality tomography. It takes advantage of microcomputed tomography and multiview bioluminescence imaging, providing anatomical structure and bioluminescence intensity information to reconstruct the size and location of tumors. By incorporating prior knowledge of signal sparsity, we associate some mathematical strategies including specific smooth convex approximation, an iterative shrinkage operator, and affine subspace with the PIS method, which guarantees the accuracy, efficiency, and reliability for three-dimensional reconstruction. Then an *in vivo* experiment on the bead-implanted mouse has been performed to validate the feasibility of this method. The findings indicate that a tiny lesion less than 3 mm in diameter can be localized with a position bias no more than 1 mm; the computational efficiency is one to three orders of magnitude faster than the existing algorithms; this approach is robust to the different regularization parameters and the l_p norms. Finally, we have applied this algorithm to another *in vivo* experiment on an HCCLM3 orthotopic xenograft mouse model, which suggests the PIS method holds the promise for practical applications of whole-body cancer detection. © 2012 Society of Photo-Optical Instrumentation Engineers (SPIE). [DOI: 10.1117/1.JBO.17.12.126012]

Keywords: iterative shrinkage; bioluminescence imaging; tumor detection; *in vivo* imaging.

Paper 12381 received Jun. 20, 2012; revised manuscript received Nov. 1, 2012; accepted for publication Nov. 8, 2012; published online Dec. 5, 2012.

1 Introduction

Molecular imaging (MI), emerging as an indispensable research tool, enhances the understanding of the physiological and pathological changes in organisms. This noninvasive technology is capable of visualizing the dynamic molecular and cellular processes taking place *in vivo* over a period of time; while the conventional route known as the gold standard is to perform a biopsy before the tissue is observed at a certain time. Hence the development of MI is of growing significance for early intervention of disease, especially for cancer, which has a global increase in incidence rate.^{1–3} There are different modalities of MI, and each modality has its own advantages, mainly varying in image resolution, detection depth, molecular sensitivity, available probes, and equipment cost.⁴ The common modalities—including ultrasound imaging, computed tomography (CT), and magnetic resonance imaging (MRI)—are generally good at detecting a lesion larger than 1 cm in diameter,⁵ while every cubic centimeter of the tumor contains approximately 0.5 to 3 billion cancer cells, which is basically too late for early detection. Thus, new imaging methods and medical equipment adapted to detect minute tumors still need to be developed.

The existing literature on multimodal fusion suggests new opportunity.^{6–8} Hereby, dual-modality tomography (DMT) has been utilized in this study, which provides multiview bioluminescence imaging (BLI) and microcomputed tomography (μ CT). BLI, one of the major modalities in optical molecular imaging, reflects the functional information by collecting the luminescent signal emitted from the internal tumor cells expressing bioluminescent proteins. Together with the anatomical structures generated by μ CT, DMT enables localization of the tumor region in three-dimensional (3-D), as well as performing a quantitative analysis. By combining the two imaging modalities, DMT therefore brings together the merits of good sensitivity, high resolution, fast speed, and low instrumentation cost, potentially making it possible for detecting liver cancer at an early stage. Since the classical imaging techniques usually depend on observing the physical properties of the tissues during diagnosis, they could hardly reveal the cellular or molecular changes associated with disease until when some obvious morphological changes occur in the lesion areas. In contrast, DMT provides higher detection sensitivity and more precise tumor localization due to the following three reasons.

1. By using specific molecular probes, DMT can explore the dynamic process of cancer development when the

Address all correspondence to: Jie Tian, Chinese Academy of Sciences, Institute of Automation, Intelligent Medical Research Center, Beijing 100190, China. Tel: +86-(10)-82628760; Fax: +86-(10)-62527995; E-mail: tian@iee.org

probes gradually bind to the targeted liver cancer cells, which ensures more sensitive detection of the miniscule tumor.

- DMT not only obtains the functional changes of living organism, but also acquires the anatomical structures such as the skeleton and organs, for the convenience of observing where tumors grow.
- DMT could visualize the complex procedures of gene expression and biological signal transmission in 3-D images, enabling the study of the characteristics and possible mechanisms of liver cancer.

For hybrid optical/ μ CT imaging, it is the 3-D reconstruction of the dual-modality data that is challenging.⁹ Reconstruction mainly refers to the procedure of creating the object in 3-D from a set of planar images, and usually a precise reconstruction result is the essential premise for the subsequent steps in image processing. In particular, DMT reconstruction involves an ill-posed inverse problem for the reason that the available information of the surface photon density is more limited than the unknown internal bioluminescence intensity, which is also regarded as an underdetermined system of linear equations. Moreover, the numerical computation of reconstruction could be time-consuming due to the large scale of three-dimensional dual-modality data, and it usually depends on selecting reconstruction parameters.

Over the past few years, the related work aiming at solving the above challenging problems has been extensively developed. To alleviate the ill-posedness and ensure reconstruction reliability, the multispectral algorithm was introduced to increase the independent boundary measurements,¹⁰ while the permissible source region approach was demonstrated to reduce the number of the unknowns.¹¹ To improve the reconstruction accuracy, classical Newton's methods with Tikhonov regularization were widely used,¹²⁻¹⁴ while they performed computationally costly to guarantee the convergence of the solution. To enhance the reconstruction efficiency, the graph cuts based methods were organized to conserve computation time due to the gradient-free optimization.^{15,16} Although the reconstruction approaches usually work well in some specific and highly controlled situations, no efforts need to be spared in investigating more general cases.¹⁷

In this paper, a parallel iterative shrinkage algorithm has been demonstrated for the dual-modality tomography, i.e., the hybrid optical/ μ CT imaging. This method has implemented the detection and visualization of the mouse liver tumors at an early stage, enabling lesion localization and its quantitative analysis. In Sec. 2, the photon diffusion model will be described mathematically, and then the principle and features of the PIS method will be introduced in detail. In Sec. 3, the feasibility and limitations of the PIS method for DMT will be thoroughly assessed, followed by the 3-D reconstruction results of the two *in vivo* experiments on mice. In Sec. 4, the conclusion and the future plan for this work will be summarized.

2 Methods

In order to compute the 3-D distributions of the lesion regions in mice, the following four steps were essentially taken to process the raw data in multiple views acquired by the DMT system. Figure 1 gives an overview of the whole procedure.

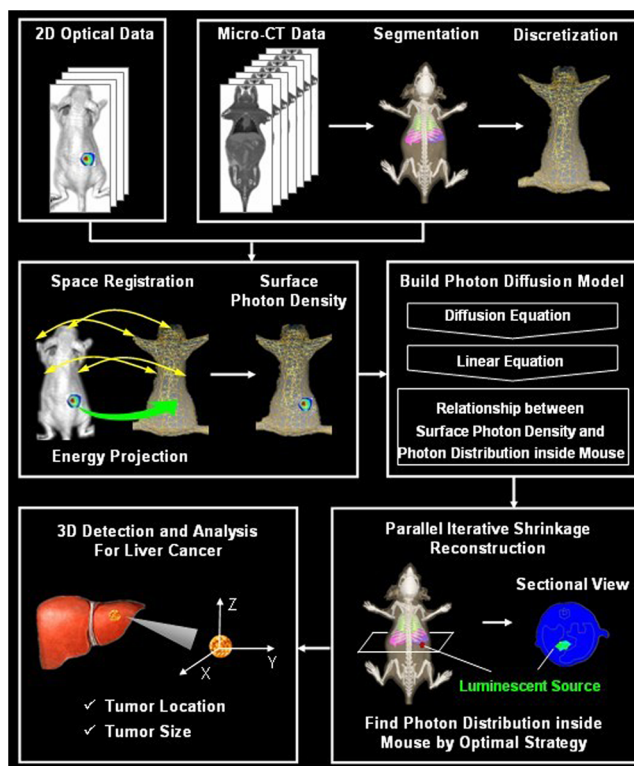


Fig. 1 The method overview. First, pre-process the raw data with segmentation, discretization, and registration; then, set up the photon diffusion model and conduct the PIS reconstruction to localize the luminescent source representing the tumor region; finally, visualize the reconstruction results in 3-D and do the necessary analysis.

- Preprocessing:** To get the 3-D photon distribution on the heterogeneous mouse surface, the raw data consisting of the planar optical images and the μ CT volume data will be processed via segmentation, discretization, space registration, and energy projection, respectively.
- Propagation model:** The diffusion equation is utilized to depict how the photons travel inside the mouse, and the finite element method is adopted to establish the linear relationship between the photon distribution on the surface and the unknown internal bioluminescence distribution inside the body.
- PIS reconstruction:** Based on the prior knowledge of signal sparsity and the optimal strategy of l_p norm minimization, the unknown bioluminescence intensity could be solved, which represents the tumor location and size.
- 3-D visualization:** To render the lesion regions inside of the mouse clearly, it is necessary to conduct the posterior tumor measurement and analysis, as well as to estimate tumor growth.

2.1 Photon Diffusion Model

The photon diffusion model describes the propagation of light through the mouse. In optical imaging, the luminescent source in the near infrared range (NIR) has low energy, leading to a diffusion-dominant transport process in a turbid medium such

as biological tissues. For this reason, the particle properties of light are mainly taken into account, including scattering and absorption; the wave nature such as polarization and interference are neglected.¹⁸ Based on those premises, the light propagation is modeled by a diffusion approximation with the Robin boundary condition.

The diffusion equation is adapted to characterize the propagation in biological tissues with the optical properties of high scattering and low absorption. It is the first-order spherical harmonics approximation for the radiative transfer equation,¹⁹ which can be written as Eq. (1) in the steady-state domain.

$$-\nabla \cdot [D(\mathbf{r})\nabla\Phi(\mathbf{r})] + \mu_a(\mathbf{r})\Phi(\mathbf{r}) = S(\mathbf{r}) \quad \mathbf{r} \in \Omega, \quad (1)$$

where D is the diffusion coefficient, and $D = \frac{1}{3[\mu_a + (1-g)\mu_s]}$; μ_a is the absorption coefficient; g is the anisotropy parameter; μ_s is the scattering coefficient; \mathbf{r} is a position vector; Φ is the photon flux density; S is the signal source distribution; Ω is the region of biological tissues.

The Robin boundary condition is employed due to the completely dark imaging environment of BLI²⁰ without any external photons, which is defined as

$$\Phi(\mathbf{r}) + 2\kappa(n)D(\mathbf{r})[v(\mathbf{r}) \cdot \nabla\Phi(\mathbf{r})] = 0 \quad \mathbf{r} \in \partial\Omega, \quad (2)$$

where κ is the boundary mismatch factor between the biological tissues and air, and $\kappa(n) = \frac{1+(1.4399n^{-2}+0.7099n^{-1}+0.6681+0.636n)}{1-(1.4399n^{-2}+0.7099n^{-1}+0.6681+0.636n)}$, n is the refractive index of the biological tissues; v is the unit outward normal on $\partial\Omega$; $\partial\Omega$ is the boundary of the biological tissues.

According to the Robin boundary condition, the theoretical outgoing photon density on the surface of the mouse is calculated by

$$T = -D(\mathbf{r})[v(\mathbf{r}) \cdot \nabla\Phi(\mathbf{r})] = \frac{\Phi(\mathbf{r})}{2\kappa(n)} \quad \mathbf{r} \in \partial\Omega, \quad (3)$$

where T is the theoretical value of the outgoing photon density on the surface.

After applying the finite element method based on the variation principle to Eqs. (1) and (2), the linear relationship can be built between the measured outgoing photon density on the surface and the bioluminescence intensity inside the body via replacing the variables with the matrix-vector forms:²⁰

$$\mathbf{MS} = \Gamma, \quad (4)$$

where \mathbf{M} is the system matrix, standing for the optical properties of the biological tissues; Γ is the measured outgoing photon density on the surface.

In Eq. (4), the photon density on surface Γ can be calculated from the multiview optical images captured by a cooled charge-coupled device. Each element of the system matrix M can be gained by Refs. 19 and 21:

$$m_{ij} = \left[\int_{\Omega_i} D(r)\nabla\varphi_i(r)\nabla\varphi_j(r)dr + \int_{\Omega_i} \mu_a(r)\varphi_i(r)\varphi_j(r)dr + \int_{\partial\Omega_i} \varphi_i(r)\varphi_j(r)/2\kappa(n)dr \right]^{-1} \int_{\Omega_i} \varphi_i(r)\varphi_j(r)dr, \quad (5)$$

where φ is the basis function in the finite element method.

Hence the procedure to solve the diffusion equation has been simplified into the form of a linear function, which can improve computational efficiency. It is peculiarly worth mentioning that Eq. (4) is an underdetermined system of linear equations with fewer equations than unknowns. This is because the available information of the surface photon density is far more limited than the unknown internal bioluminescence intensity, consequently causing difficulties in the following 3-D reconstruction.

2.2 Prior Knowledge and Optimal Strategy

The DMT reconstruction is involved in solving an undetermined system of linear equations, which is mathematically considered to be an ill-posed problem on account of its infinite solutions. In order to reduce the ill-posedness, *a priori* knowledge known as a sparse constraint is introduced, by which an approximation close to the exact solution can be eventually found. Since this paper emphasizes the detection of early-stage tumors, there usually turns out to be sparse signals in the biological organism,²² referring to a distribution with a large number of zeros except for minimal support of the solution space that denotes the lesion areas. Thus the methods for sparse signals recovery (SSR) offer valuable alternatives to DMT reconstruction.

The essence of SSR is to utilize the limited linear observations via a normal optimal strategy. Since the samples required by SSR could be less than the quantity needed by the Nyquist sampling theorem, the underdetermined system of equations can be solved by finding the best basis that stands for the bioluminescence intensity. A number of iterative algorithms,^{23–27} which have been developed to retrieve sparse signals include the Born iterative method, Truncate-Newton, Levenberg-Marquardt approach, etc.

Furthermore, a regularization strategy was also exploited for DMT reconstruction. Generally, the simplest solution to Eq. (4) is in the form of the least square expressed as Eq. (6), but it tends to amplify the errors generated by noise. In order to make the reconstruction more practical, a constraint condition known as a regularization term is added. For instance, one of the most commonly used methods named Tikhonov regularization considers the l_2 norms constraint for the unknown internal source,²⁸ the form of which is written in Eq. (7). Although this method can optimize the results, it still leads to the over-smooth problem, which blurs the reconstructed source boundary and misses part of the source information.

$$\operatorname{argmin}_S \left[\frac{1}{2} \|\mathbf{MS} - \Gamma\|_2^2 \right] \quad (6)$$

$$\operatorname{argmin}_S \left[\frac{1}{2} \|\mathbf{MS} - \Gamma\|_2^2 + \lambda \|S\|_2^2 \right], \quad (7)$$

where λ is the regularization parameter.

To overcome the above difficulties, we incorporated the sparse signals as the prior knowledge and used a more generalized form for the constraint condition, the l_p norm regularization term, shown in Eq. (8). So far, the optimal object function for retrieving the DMT signals has been obtained, which is a linear inverse problem formulated as Eq. (9). The internal source distribution representing the tumor region can be ultimately determined by solving the object function via optimal minimization in the next section.

$$\operatorname{argmin}_S \left[\frac{1}{2} \|\mathbf{MS} - \Gamma\|_2^2 + \lambda \|S\|_p^p \right] \quad (8)$$

$$f(S) = \frac{1}{2} \|\mathbf{MS} - \Gamma\|_2^2 + \lambda \|S\|_p^p, \quad (9)$$

where $\|\cdot\|_2$ stands for the l_2 norm; $\|\cdot\|_p$ stands for the l_p norm; p is a real number in the range from one to two.

2.3 Parallel Iterative Shrinkage Algorithm

The iterative shrinkage strategy is a newly emerged numerical computational method. It surpasses the traditional iteration optimization such as the steepest-descent, the conjugate gradient and the interior-point²⁹⁻³¹ in terms of temporal and spatial efficiency particularly when solving the multidimension problem. Because of those strengths, the iterative shrinkage methods have recently been applied to image denoising and the inverse problem.³²

The PIS approach, belonging to the iterative shrinkage methods,³³ intrinsically converts a complex process of optimizing the multidimension function into a set of parallel one-dimension optimizations with respect to each variable. In other words, the full set of unknown variables is iteratively optimized at the same time instead of being updated sequentially, by which the computational complexity can thereby be simplified.

To further illustrate how such an algorithm fits into DMT reconstruction, we mathematically derived the PIS method using the following four steps.

Step 1: To simplify the object function from multiple dimensions to one dimension with the iterative shrinkage strategy. Assuming that within an individual iteration of optimization, we have the k 'th estimate for the internal source distribution s_k . To calculate the next estimate s_{k+1} , α stands for the j 'th element where $s_{k+1}(j)$ is updated by Eq. (10), supposing all of the other elements are fixed. Afterward, the object function originally has x dimensions, then Eq. (9) will be converted into the form of the dimension referred to in Eq. (11).

$$\alpha = \operatorname{argmin}_\alpha \frac{1}{2} \|\mathbf{M}s_k - \Gamma - m_j s_k(j) + m_j \alpha\|_2^2 + \lambda \|\alpha\|_p^p \quad (10)$$

$$g(\alpha) = \frac{1}{2} \|\mathbf{M}s_k - \Gamma - m_j [s_k(j) - \alpha]\|_2^2 + \lambda \|\alpha\|_p^p, \quad (11)$$

where k is a natural number; j is a natural number; s_k is the k th estimate of the internal source distribution S ; $s_k(j)$ is the j th element in s_k ; α stands for $s_{k+1}(j)$; m_j is the j th column element in the system matrix \mathbf{M} .

Step 2: To achieve the analytical solution by introducing a smooth convex approximation. Since the analytical solution to the object function does not exist by directly taking the derivative of Eq. (11), the regularization term can be replaced with the smooth convex approximation $\theta(w)$, a differentiable function defined in Eq. (12). It fits the regularization term appropriately while the two variables, w and p , remain as the relationship shown in Fig. 2. Then the object function can be modified as Eq. (13). To minimize it, take the first derivative of the equation with respect to α and set it to zero, yielding Eq. (14). Rewrite it as Eq. (15), which is a quadratic equation, so that α can therefore be analytically solved.

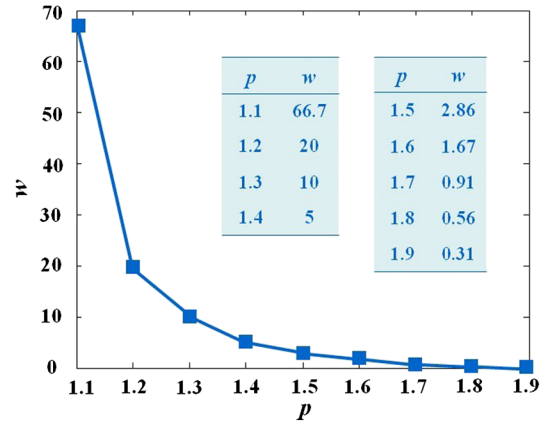


Fig. 2 The relationship curve between w and p , providing several pairs of their coordinates.

$$\theta(w) = \frac{1}{2} [\|\alpha\|_1 - w \ln(1 + \|\alpha\|_1/w)] \quad (12)$$

$$g(\alpha) = \frac{1}{2} \|\mathbf{M}s_k - \Gamma - m_j [s_k(j) - \alpha]\|_2^2 + \lambda \theta(w) \quad (13)$$

$$m_j^T [\mathbf{M}s_k - \Gamma - m_j s_k(j) + m_j \alpha] + \lambda \frac{\alpha}{w + \alpha} = 0 \quad (14)$$

$$\begin{cases} \alpha^2 + (\beta + w + \lambda)\alpha + w\beta = 0 \\ \beta = m_j^T (\mathbf{M}s_k - \Gamma) - s_k(j) \end{cases}, \quad (15)$$

where $\theta(w)$ is a smooth convex approximation function; w is a positive real number.

Step 3: To accelerate the reconstruction using an iterative shrinkage operator, which can be computed in parallel. The expression of the specific iterative shrinkage operator $H_k(j)$ is given by Eq. (16). Apparently its calculation will be activated once the values of λ and w are set. Since the elements of $H_k(j)$ are independent of each other, they can be simultaneously obtained with the help of Eq. (17), thus enhancing reconstruction efficiency.

$$\begin{cases} H_k(j) = \frac{(V_j - w - U_j) + \sqrt{(|V_j| - w - U_j)^2 + 4w|V_j|}}{2\operatorname{sign}(V_j)} \\ V_j = m_j^T (\Gamma - \mathbf{M}s_k) / \|m_j\|^2 + s_k(j), \quad U_j = \lambda / \|m_j\|^2 \end{cases} \quad (16)$$

$$\begin{cases} H_k = \frac{(V - w - U) + \sqrt{(|V| - w - U)^2 + 4w|V|}}{2\operatorname{sign}(V)} \\ V = \operatorname{diag}^{-1}(\mathbf{M}^T \mathbf{M}) \mathbf{M}^T (\Gamma - \mathbf{M}s_k) + s_k \\ U = \lambda \operatorname{diag}^{-1}(\mathbf{M}^T \mathbf{M}) \end{cases} \quad (17)$$

where “sign” stands for the sign function; “diag” stands for extracting the diagonal elements of a matrix.

Step 4: To compute the next iterative estimate via an affine subspace optimization. For any iterative optimal strategy, it is essentially required to select the optimal direction d_k and the step length σ_k when searching for the next iterative estimate s_{k+1} , because they can usually ensure a more accurate result. Instead of using the classical linear search, the affine subspace D_k defined in Eq. (18) is employed here to aid

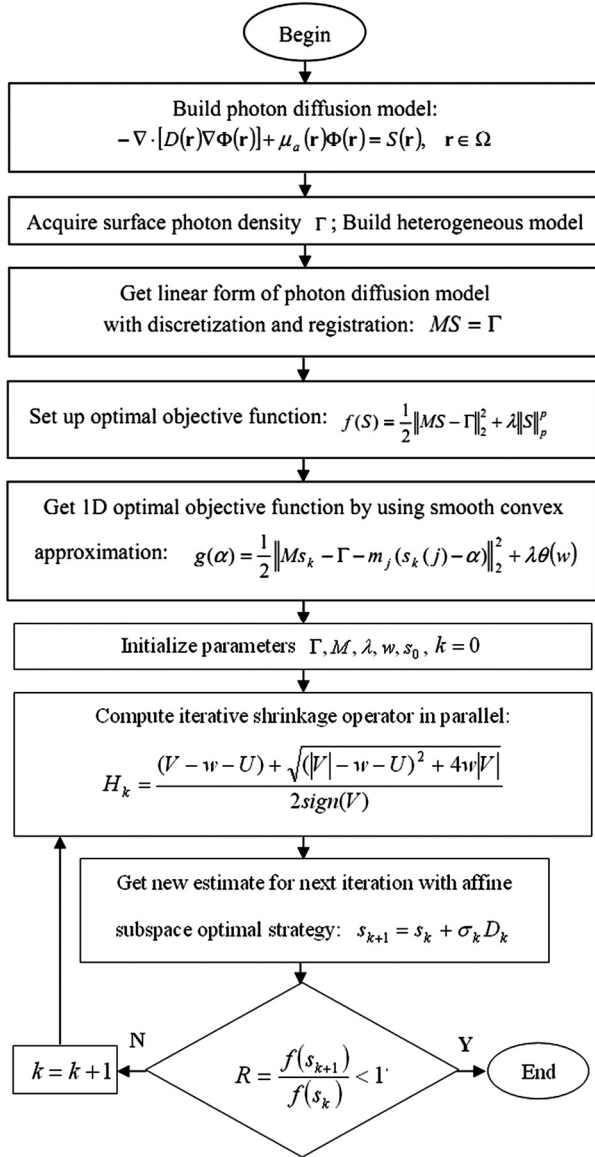


Fig. 3 The flowchart of the PIS algorithm for the DMT reconstruction.

the decision of the next direction for optimization. It is compromised of the previous directions as well as being based on the iterative shrinkage operator mentioned in the former step. In addition, the step length of the next iteration can be acquired by Eq. (19), consequently enabling the computation of s_{k+1} in Eq. (20). The iterative optimization will stop when the ratio $R = g(s_{k+1})/g(s_k) < 0.1$ is satisfied, and DMT reconstruction results denoting the internal source distribution S will be ultimately achieved

$$\begin{cases} D_k = \{d_k^i\}_{i=1}^k \\ d_k^1 = H_k - s_k \\ d_k^i = s_{k-i+1} - s_{k-i} \quad (i = 2, 3, \dots, k) \end{cases} \quad (18)$$

$$\sigma_k = \underset{\sigma}{\operatorname{argmin}} g(s_k + \sigma D_k) \quad (19)$$

$$s_{k+1} = s_k + \sigma_k D_k, \quad (20)$$

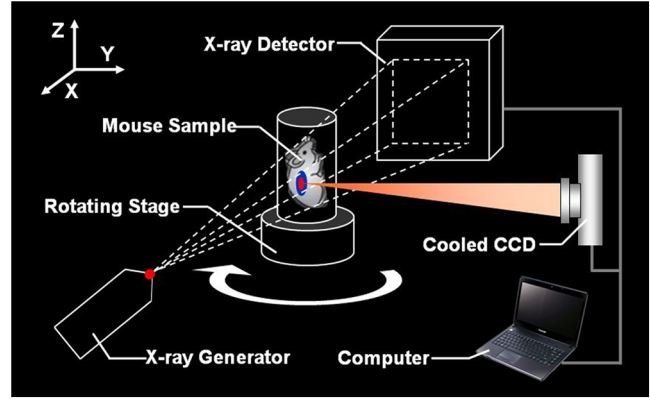


Fig. 4 The schematic illustration of the DMT system. It provides multi-view BLI and μ CT, the major devices of which are illustrated in Table 1.

Table 1 The manufacturers and models for the components of the DMT system.

| Device | Manufacturer and model |
|-----------------|--|
| Cooled CCD | Princeton instruments, PIXIS: 1024 |
| CCD lenses | Nikon Nikkor, 50 mm f1.2 |
| X-ray generator | Oxford Instruments, 90 kV UltraBright Micro-focus Source |
| X-ray detector | Hamamatsu Photonics, C7943CA-02 Flat Panel Sensor |
| Rotating stage | Beijing Zolix Instruments, RAK |

where D is the affine subspace; d is the direction of an iteration; i is a positive integer, ranging from two to k ; σ is the step length of an iteration.

In summary, the PIS algorithm for the DMT reconstruction can be concisely demonstrated by the flowchart in Fig. 3.

3 Results and Discussion

To validate the feasibility of the PIS method for the DMT reconstruction, an *in vivo* experiment on the nude mouse that was implanted with a plastic luminescent bead in the liver has been conducted using the hybrid optical/ μ CT imaging system developed by our group.³⁴ Then we have applied the proposed approach to another *in vivo* experiment on an HCCLM3 orthotopic xenograft mouse model. Note that HCCLM3 stands for a human hepatocellular carcinoma cell line with high metastatic potential.

3.1 Dual-Modality Imaging System Setup

The DMT system, surrounded in a completely dark environment, provides two modalities: multiview BLT and μ CT. The schematic illustration of the system is given by Fig. 4, which is mainly equipped with a cooled CCD, a set of optical lenses, an x-ray generator, an x-ray detector, and a rotating stage (the manufacturers and models are listed in Table 1). This system enables noninvasive *in vivo* imaging for small animals, making it possible to observe the dynamic biological behavior in real

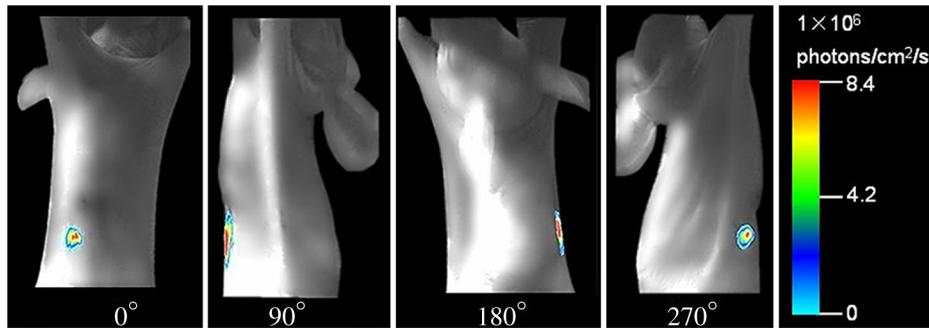


Fig. 5 The multi-view BLI data of the experimental nude mouse with an implanted luminescent bead. Four pictures taken at 0 deg, 90 deg, 180 deg, and 270 deg by the cooled CCD.

time. However, if detecting the same activity taking place in the body by the conventional method, a group of experimental mice have to be sacrificed for the inevitable pathological section analysis. Besides reducing the quantity of the experimental animals, this new hybrid imaging method can also result in more reliable datasets since the whole dynamic procedure can be achieved on the same mouse, thus avoiding individual differences.

3.2 Data Acquisition and Image Preprocessing

Prior to the experiment, the dual-modality raw data was collected, respectively. The acquisition time for the entire procedure was within 10 min, which could be tolerated by the mice. As delineated in Fig. 4, the mouse was firstly placed on the automatic rotating stage. Afterward, the photons emitted from the mouse body were captured in four different views by the cooled CCD. The four planar optical images are displayed in Fig. 5. At last, the cone-beam μ CT projection data with 360-deg views was scanned using the x-ray generator and the detector.

After achieving the raw data, some necessary preprocessing operations were carried out to make the data suitable for posterior reconstruction.

- (1) μ CT Reconstruction: The cone-beam μ CT projection data was reconstructed by the GPU accelerated

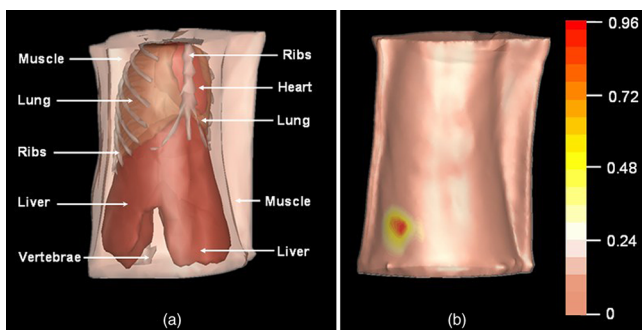


Fig. 6 The heterogeneous volume data and the surface photon distribution of the experimental nude mouse with an implanted luminescent bead. (a) The volume data of the heterogeneous mouse model after the segmentation of the major organs and tissues including the heart, lungs, liver, muscle, and skeleton; (b) the surface photon distribution of the mouse body after registration, where the photons are assembled as a bright spot on the bottom left. Compared with (a), it could be estimated that the spot is close to or located exactly at the liver region.

Feldkamp-Davis-Kress (FDK) algorithm³⁵ to yield the mouse volume data in 3-D

- (2) Segmentation: To build the heterogeneous mouse model delineated in Fig. 6(a), the major organs and tissues were segmented including the heart, lungs, liver, muscle, and skeleton
- (3) Discretization: The mouse body was discretized into a volumetric mesh containing 4,560 nodes and 23,752 tetrahedral elements
- (4) Registration: To portray the photon distribution on the body surface depicted in Fig. 6(b), the optical images were mapped onto the surface of the volumetric mesh in terms of space and energy.

3.3 In Vivo Experiment on the Bead-Implanted Mouse

The experimental nude mouse's liver in this section was surgically implanted with the luminescent bead. Anterior to imaging, the mouse was injected through the caudal tail vein with 0.3-ml

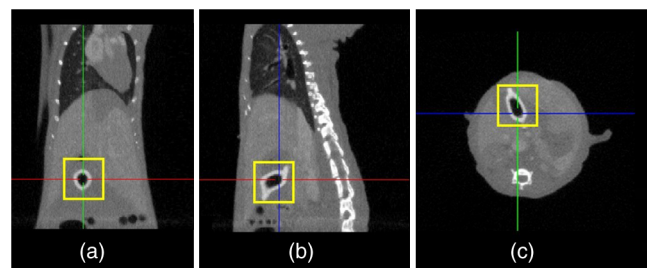


Fig. 7 Three slices of the μ CT data, where the yellow square marks the location of the luminescent bead: (a) the coronal view; (b) the sagittal view; (c) the transversal view.

Table 2 The optical properties of the mouse organs and tissues (mm^{-1}), where the first row represents the absorption coefficient, while the second row denotes the scattering coefficient.

| | Lungs | Heart | Liver | Muscle | Skeleton |
|---------|--------|--------|--------|--------|----------|
| μ_a | 0.022 | 0.071 | 0.128 | 0.075 | 0.032 |
| D | 0.2896 | 0.1403 | 0.4307 | 0.1480 | 0.5394 |

Fenestra vascular contrast agent to enhance the μ CT images, followed by 0.3 ml of anesthetic at a 0.15 g/ml concentration via intraperitoneal injection. When the anesthetic set in, an irregular-shaped bead the size of $2.10 \times 2.70 \times 2.40$ mm was embedded into the mouse. This luminescent source was suited for stimulating the liver tumor inside the living organism, because its wavelength ranged from 650 to 700 nm, which is identical to that of the light produced by firefly luciferase. It is worth mentioning that this study could examine the reconstruction accuracy of the PIS method, because the luminescent bead was wrapped in a plastic material, which could be easily detected by μ CT.

After acquiring the raw data using the DMT system, the μ CT data was reconstructed into the volume data, three slices of which are shown in Fig. 7, where the square marks the location of the luminescent bead at the coordinate (24.6, 20.0, 7.2). After combining the optical data displayed in Fig. 5, the heterogeneous volume and the surface photon distribution shown in Fig. 6 could be therefore achieved. To distinguish the different optical properties of the organs and tissues, the adding-doubling technique³⁶ was utilized to improve the heterogeneous mouse model, where the organs and tissues were assigned the corresponding coefficients of absorption and scattering in Table 2. Finally, the reconstruction based on the PIS method was performed to localize where the luminescent bead was inside the mouse body. The reconstruction results will be evaluated in more detail in the next section.

3.4 Evaluation of Reconstruction Accuracy

To validate the reconstruction accuracy of the PIS approach, comparisons were made between the reconstructed internal

source and the plastic luminescent bead. Figure 8 gives the results in the case when $\lambda = 10^{-3}$ and $p = 1.1$, demonstrating the size of the reconstructed source and its location to the organs and tissues inside the mouse body.

It can be seen from Fig. 8(a) that the reconstructed source is located in the liver region, and the coordinate of the source center is (24.0, 19.8, 7.4). To display the entire source more clearly, the liver was concealed in Fig. 8(b), enabling the measurement of the source size, which was $2.41 \times 2.31 \times 2.93$ mm. In addition, Fig. 8(c) shows the sectional view of the μ CT slice where the center of the luminescent bead was located, which was visually in good agreement with the center of the reconstructed source shown in Fig. 8(d). A further computation confirmed that the position bias between the two centers was approximately 0.66 mm.

The above results suggest the lesion region was less than 3 mm in diameter but could be detected by means of the PIS method, with a position bias no more than 1 mm.

3.5 Evaluation of Reconstruction Efficiency

To examine the reconstruction efficiency of the PIS algorithm, take the same case as an example. Figure 8(e) describes the convergence speed of the iterative reconstruction with the same parameters mentioned in the former section. It is noted that the iterative curves still resemble each other even when the parameters are changed. During the total 40 iterations, the value of the optimal object function decreased substantially, moving towards an ultimate convergence. The whole procedure of this reconstruction cost 9.82 s. In particular, the value tended to be zero as early as the 20th iteration, and then it became more stable.

Moreover, the classical Newton's algorithm and the generalized graph cut (GGC) approach were also applied to reconstruct the same dataset.³⁷ The comparison of the reconstruction efficiency was made based on the data in Table 3. It shows the time consumed by the two different methods as well as the proposed one for reconstructing the four groups of datasets whose sizes are determined by the density of the discrete volumetric mesh.

The results reveal that: 1. When reconstructing the same dataset, the GGC approach works more efficiently than Newton's algorithm, but is less efficient than the proposed PIS method; 2. When the size of the dataset increases, the PIS method becomes more computationally competitive; 3. all of the datasets are discretized based on the whole mouse torso, which means the proposed method is not only time efficient, but also has the potential for practical applications.

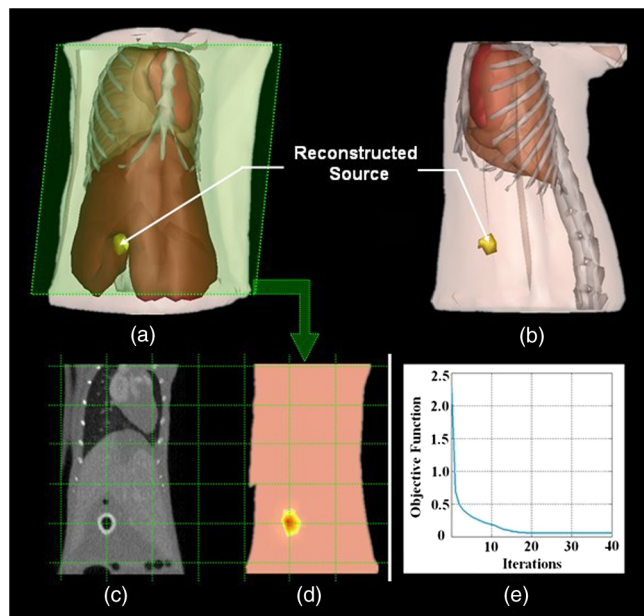


Fig. 8 The reconstruction results using the PIS method in the case when $\lambda = 10^{-3}$ and $p = 1.1$: (a) the front view in 3-D; (b) the side view in 3-D while setting the liver region as invisible; (c) the coronal view of the μ CT slice where the center of the luminescent bead was located; (d) the sectional view of the DMT reconstruction results where the reconstructed internal source was located; (e) the corresponding iterative curve, reflecting the convergence speed of the reconstruction.

Table 3 The comparison of the reconstruction efficiency based on different methods. The size of the volumetric mesh equals the number of nodes multiplied by the number of tetrahedral elements.

| No | Volumetric mesh size | Newton's | GGC | PIS |
|----|----------------------|------------|----------|--------|
| 1 | 2,125 × 7,761 | 817.86 s | 39.88 s | 3.34 s |
| 2 | 3,048 × 15,890 | 2,294.66 s | 68.58 s | 4.81 s |
| 3 | 3,714 × 17,218 | 4,931.42 s | 146.17 s | 7.47 s |
| 4 | 4,560 × 23,752 | 7,891.52 s | 345.74 s | 9.82 s |

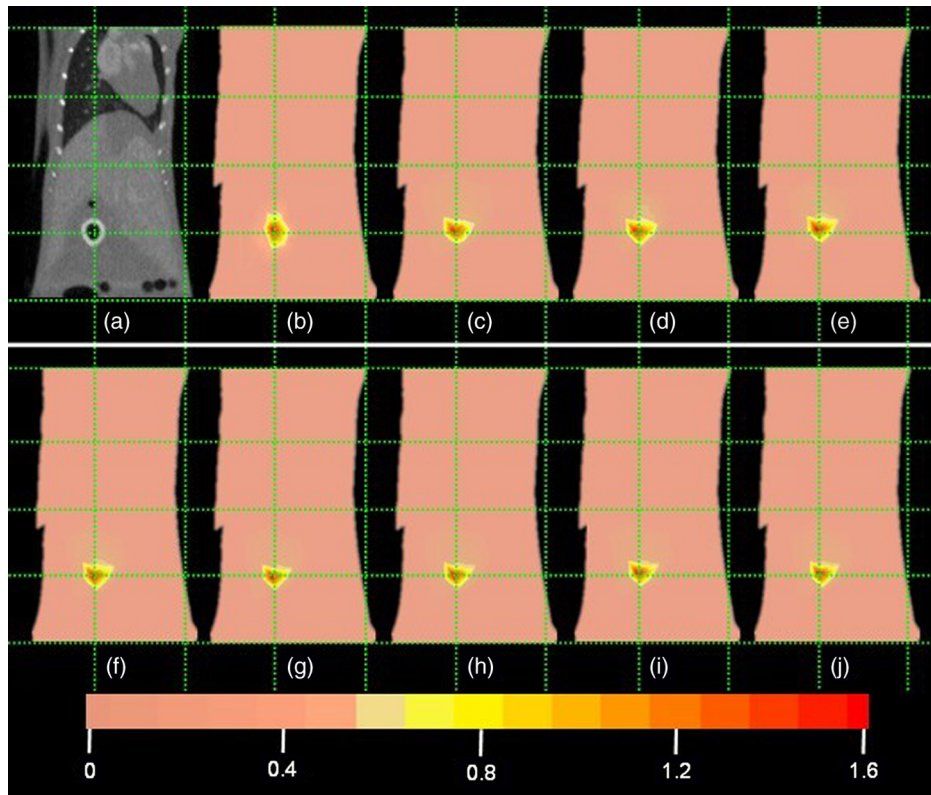


Fig. 9 The comparisons of the reconstruction results in sectional views with different regularization parameters λ : (a) the coronal view of the μ CT slice where the center of the luminescent bead was located; (b) to (j) the sectional views of the reconstruction results in the cases when $\lambda = 10^{-3}, 10^{-5}, 10^{-7}, 10^{-9}, 10^{-11}, 10^{-13}, 10^{-15}, 10^{-17}, 10^{-19}$, respectively, while maintaining the same p value, $p = 1.1$.

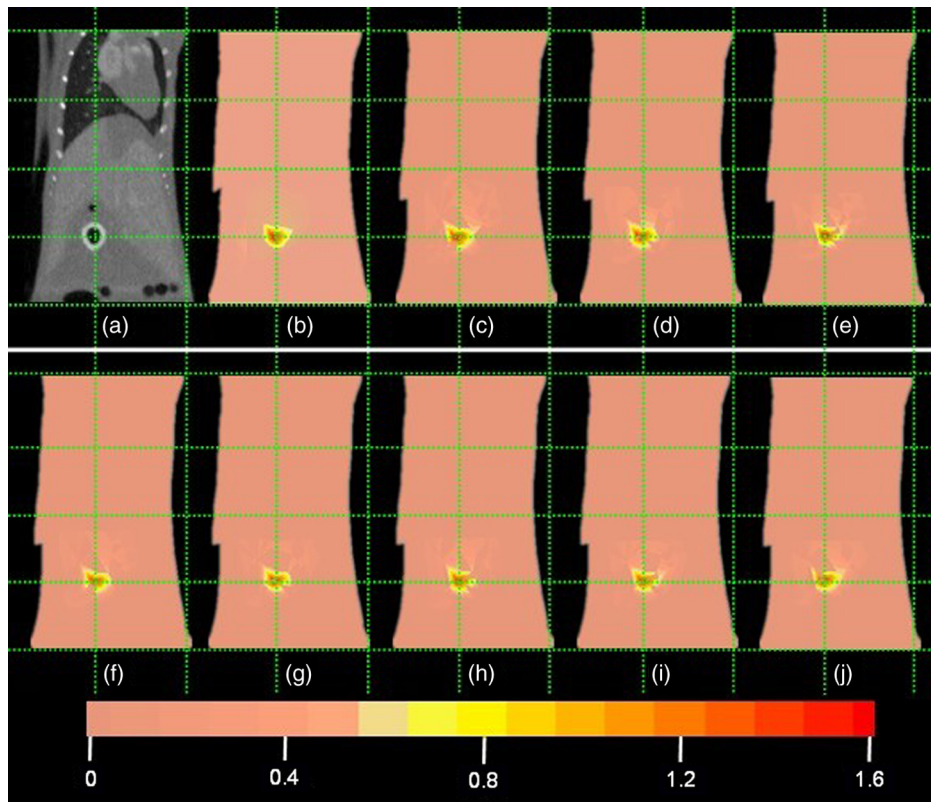


Fig. 10 The comparisons of the reconstruction results in sectional views with a different l_p norm: (a) the coronal view of the μ CT slice where the center of the luminescent bead was located; (b) to (j) the sectional views of the reconstruction results in cases when $p = 1.1, 1.2, 1.3, 1.4, 1.5, 1.6, 1.7, 1.8, 1.9$, respectively, while maintaining the same λ value, $\lambda = 10^{-5}$.

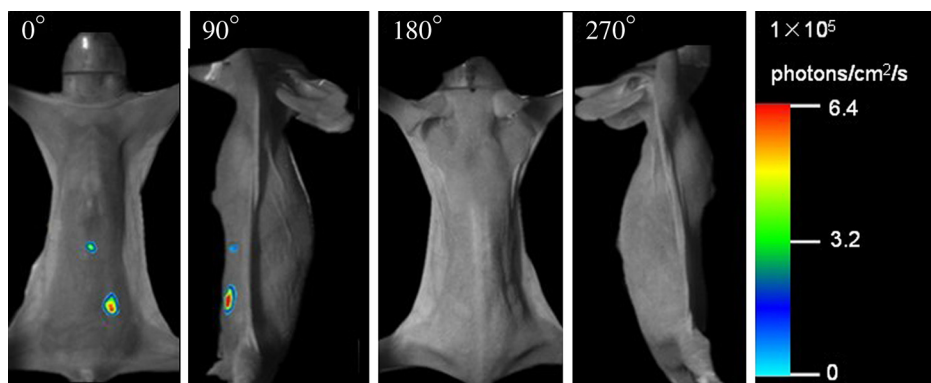


Fig. 11 The multi-view BLI data of the HCCLM3 orthotopic xenograft mouse model. Four pictures take at 0 deg, 90 deg, 180 deg, and 270 deg via the cooled CCD.

3.6 Evaluation of Reconstruction Reliability

To verify the reconstruction reliability of the PIS method, we have conducted 180 reconstructions for testing its tolerance with different parameters. Generally speaking, the reconstruction accuracy is considerably affected by the regularization parameter λ and the l_p norm, where slight changes may dramatically have an impact on the results. In this section, the regularization parameter $\lambda = 10^{-n}$ was selected with different orders of magnitude, with n ranging from 1 to 20; as for the l_p norm, p was chosen to be between 1.1 and 1.9. The sectional views of the reconstruction results are partly delineated in Figs. 9 and 10.

Comparing the locations between the luminescent bead in Fig. 9(a) and the reconstructed bright spots in Fig. 9(b) to 9(j), we found that they were visually in good agreement by virtue of the auxiliary grid. Further computation revealed that the position bias in each reconstruction was less than 1 mm, and more details have been explored about the position bias. 1. It reaches the lowest peak when $\lambda = 10^{-3}$; 2. it maintains a smaller value when $\lambda < 10^{-3}$, ensuring satisfying results; 3. it rises substantially when $\lambda > 10^{-3}$, meaning undesirable options. Therefore the proposed algorithm is robust to a wide variety of parameters, whereas the regularization parameter λ could be no more than 10^{-3} , and the norm p has a more flexible selection.

3.7 In Vivo Experiment on HCCLM3 Orthotopic Xenograft Mouse Model

Unlike the experimental mouse introduced in Sec. 3.3, the nude mouse in this section was an orthotopic xenograft model inoculated with HCCLM3 cell lines. Those fLuc-expressing HCCLM3 cell lines are suitable for BLI.

Before imaging, both the anesthetic and luciferine were successively injected into the mouse, where the photons were emitted during the oxidation reaction on the condition that luciferase met luciferine. The amount of the outgoing photons collected by the DMT system is linearly correlated to the quantity of the liver cancer cells inside the mouse, because the chemical reaction will occur only when the cancer cells are alive, and only one photon will be sent out every time when the reaction works.

During imaging, the optical images in the four views were attained by the BLI modality, and the volume data at 360 deg was scanned by the μ CT modality. The accumulated acquisition time was about 7 min in total, in which each optical

image took 10 s of the integral time while the μ CT scanning cost 60 s. The raw optical pictures in Fig. 11 describe the photon distribution in two-dimensional (2-D) of the whole mouse, where two bright spots could be caught from 0 deg and 90 deg, but not from obviously visible luminescence at 180 deg and 270 deg. After imaging, the mouse was subjected to laparotomy and was analyzed using H&E staining, and lesions could be observed in the liver region.

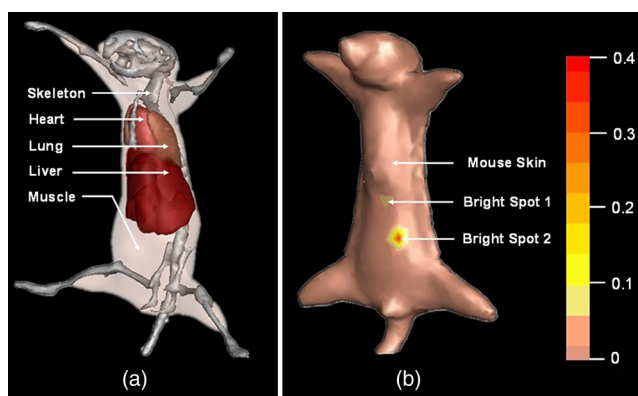


Fig. 12 The heterogeneous volume data and the surface photon distribution of the HCCLM3 orthotopic xenograft mouse model: (a) the volume data of the heterogeneous mouse model after the segmentation of the major organs and tissues including the heart, lungs, liver, muscle, and skeleton; (b) the surface photon distribution of the mouse body after registration.

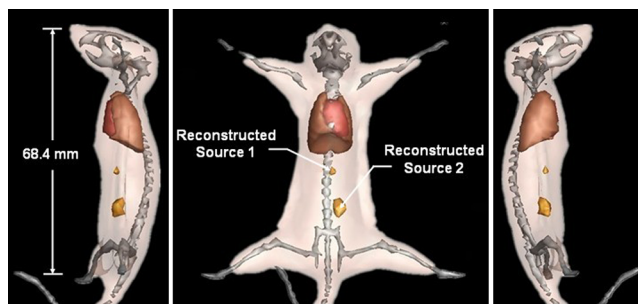


Fig. 13 The reconstruction results of the HCCLM3 orthotopic xenograft mouse model using the PIS method in case when $\lambda = 10^{-3}$ and $p = 1.1$, including a front view and two side views.

Prior to reconstruction, the dual-modality data was preprocessed. After segmentation, the μ CT volume of the whole mouse is shown in Fig. 12(a), which clearly depicts the anatomical structure in 3-D, but the tumor could be hardly observed due to the limitations of μ CT, such as the low contrast for detecting soft tissues. After registration, the 2-D photon distribution was mapped onto the surface of the 3-D volume data. From Fig. 12(b), we can notice that there are two bright spots on the surface of the mouse abdomen, consisting of the gathered photons emitted from the internal liver tumors, but it could neither offer the 3-D distribution of the internal tumors, nor suggest how they were located in relation to the organs and tissues inside the mouse's body. That is why the following reconstruction based on the PIS approach is essential.

When the reconstruction was performed, the whole mouse volume data was discretized into a volumetric mesh containing 5193 nodes and 53,653 tetrahedral elements. Figure 13 describes the results in the case when $\lambda = 10^{-3}$ and $p = 1.1$, where the reconstruction time is 9.83 s. The liver region is set to be invisible in order to not cover the reconstructed tumors, and it can be perceived that there are two tumors inside the mouse's body. The smaller one measures about $1.64 \times 1.30 \times 2.10 \text{ mm}^3$, and the volume of the larger one is around $3.45 \times 3.83 \times 5.31 \text{ mm}^3$.

The above findings suggest that the PIS method is able to detect the lesions in the above biomedical application, and two liver tumors have been localized at the same time in the HCCLM3 orthotopic xenograft mouse model.

4 Conclusions and Future Work

The PIS reconstruction algorithm proposed in this research project is capable of enhancing accuracy efficiency, and reliability in whole-body liver cancer detection mainly using the following three strategies:

- (1) An affine subspace compromised of the previous direction, which has been employed to compute the next iterative estimate, instead of using classical linear search, which could precisely aid the decision of the direction for optimization, ensuring the reconstruction accuracy.
- (2) An iterative shrinkage strategy has been utilized to simplify the problem from multiple dimensions to a single dimension, which is associated with an iterative shrinkage operator that can be computed in parallel to accelerate the reconstruction efficiency.
- (3) A smooth convex approximation which has been proposed to represent the l_p norm regularization term, a more generalized form for the constraint condition, so that the analytical solution to the optimal object function can be achieved to enhance the reliability of this method.

In addition, two *in vivo* experiments on nude mice have been conducted to evaluate the feasibility and limitations of the proposed method in liver cancer detection. The results indicate that:

- (1) The DMT technique is not only sensitive in finding the smaller lesions, which usually cannot be discovered if using the single μ CT modality, but also capable of quantitatively measuring the tumor size

and visualizing its location in the organs and tissues inside the mouse body in 3-D.

- (2) The PIS approach has been verified by the experiment on a bead-implanted mouse, so it could localize a tumor that is less than 3 mm in diameter with a position bias less than.
- (3) The computational efficiency of the proposed reconstruction algorithm has been improved by one to three orders of magnitude in contrast to the classical approaches, and it becomes more computationally competitive as the dataset size increases.
- (4) The reconstruction reliability of the PIS method has been proven in that it has a good tolerance with different parameters, where the regularization parameter λ could be no more than 10^{-3} , and the norm p has a more flexible selection.
- (5) The potential of the proposed method for practical application has been further validated in the experiment on the HCCLM3 orthotopic xenograft mouse model, where two small lesions less than 1 mm in diameter have been found by the whole-body reconstruction.

Future work will emphasize on improving the drawbacks of the proposed PIS algorithm. Despite tumor size, which could only be measured approximately, it is still difficult in achieving an accurate tumor boundary, which is critically important for surgical removal. This is because FEM was employed to establish the photon diffusion model in this study, and it is fundamentally limited in describing the shape of objects. On the other hand, the second experiment could be extended further. It deserves more in-depth studies of the weak signals from the internal cancer cells, as well as tumor metastasis resulting in more internal luminescent sources instead of only one or two, so that the whole-body reconstruction for multisource mouse model can be done better.

Acknowledgments

This study was supported by the National Basic Research Program of China (973 Program) under Grant No. 2011CB707700, the Knowledge Innovation Project of the Chinese Academy of Sciences under Grant No. KGCX2-YW-907, the National Natural Science Foundation of China under Grant Nos. 81227901, 61231004, 81027002, 81261120414, the Chinese Academy of Sciences Visiting Professorship for Senior International Scientists under Grant No. 2012T1G0036, and the Beijing Natural Science Foundation No. 4111004.

References

1. R. Weissleder and J. M. Pittet, "Imaging in the era of molecular oncology," *Nature* **452**(7187), 580–589 (2008).
2. A. Morabia and T. Abel, "The WHO report 'Preventing chronic diseases: a vital investment' and us," *Soz Präventivmed.* **51**(2), 74–74 (2006).
3. A. Jemal et al., "Global cancer statistics," *CA: A Cancer J. Clin.* **61**(2), 69–90 (2011).
4. T. F. Massoud and S. S. Gambhir, "Molecular imaging in living subjects: seeing fundamental biological processes in a new light," *Genes Dev.* **17**(5), 545–580 (2003).

5. A. Muhi et al., "Diagnosis of colorectal hepatic metastases: comparison of contrast-enhanced CT, contrast-enhanced US, superparamagnetic iron oxide-enhanced MRI, and gadoteric acid-enhanced MRI," *J Magn. Reson. Imaging* **34**(2), 326–335 (2011).
6. H. Fan-Minogue et al., "Noninvasive molecular imaging of c-Myc activation in living mice," *Proc Natl. Acad. Sci.* **107**(36), 15892–15897 (2010).
7. M. Nahrendorf et al., "Hybrid PET-optical imaging using targeted probes," *Proc Natl. Acad. Sci.* **107**(17), 7910–7915 (2010).
8. A. Ale et al., "FMT-XCT: *in vivo* animal studies with hybrid fluorescence molecular tomography-X-ray computed tomography," *Nat. Methods* **9**(6), 615–620 (2012).
9. V. Ntziachristos, "Going deeper than microscopy: the optical imaging frontier in biology," *Nat. Methods* **7**(8), 603–614 (2010).
10. C. Kuo et al., "Three-dimensional reconstruction of *in vivo* bioluminescent sources based on multispectral imaging," *J. Biomed. Opt.* **12**(2), 024007 (2007).
11. Y. Lu et al., "A multilevel adaptive finite element algorithm for bioluminescence tomography," *Opt. Express* **14**(18), 8211–8223 (2006).
12. J. Tian et al., "Multimodality molecular imaging—improving image quality," *IEEE Eng. Med. Biol. Mag.* **27**(5), 48–57 (2008).
13. Y. Lu et al., "Source reconstruction for spectrally-resolved bioluminescence tomography with sparse *a priori* information," *Opt. Express* **17**(10), 8062–8080 (2009).
14. G. Wang et al., "*In vivo* mouse studies with bioluminescence tomography," *Opt. Express* **14**(17), 7801–7809 (2006).
15. K. Liu et al., "A fast bioluminescent source localization method based on generalized graph cuts with mouse model validation," *Opt. Express* **18**(4), 3732–3745 (2010).
16. P. Rodríguez and B. Wohlberg, "Efficient minimization method for a generalized total variation functional," *IEEE Trans. Image Process.* **18**(2), 322–332 (2009).
17. N. Blow, "*In vivo* molecular imaging: the inside job," *Nat. Methods* **6**(6), 465–469 (2009).
18. L. V. Wang and H. I. Wu, *Bio Opt: Principles and Imaging*, John Wiley and Sons, Hoboken (2007).
19. W. X. Cong et al., "Practical reconstruction method for bioluminescence tomography," *Opt. Express* **13**(18), 6756–6771 (2005).
20. S. R. Arridge, "Optical tomography in medical image," *Inverse Probl.* **15**(2), R41–R93 (1999).
21. M. Schweiger et al., "The finite element method for the propagation of light in scattering media: boundary and source conditions," *Med. Phys.* **22**(11), 1779–1792 (1995).
22. S. S. Chen, D. L. Donoho, and M. A. Saunders, "Atomic decomposition by basis pursuit," *SIAM J. Sci. Comput.* **20**(1), 33–61 (1998).
23. J. C. Ye et al., "Modified distorted Born iterative method with an approximate Frechet derivative for optical diffusion tomography," *J. Opt. Soc. Amer.* **16**(7), 1814–1826 (1999).
24. Y. Q. Yao et al., "Frequency-domain optical imaging of absorption and scattering distributions by a born iterative method," *J. Opt. Soc. Amer.* **14**(1), 325–342 (1997).
25. R. Roy and E. Sevick-Muraca, "Truncated newton's optimization scheme for absorption and fluorescence optical tomography: part I theory and formulation," *Opt. Express* **4**(10), 353–371 (1999).
26. M. Schweiger, S. R. Arridge, and D. T. Delpy, "Application of the finite-element method for the forward and inverse models in optical tomography," *J. Math. Imaging Vis.* **3**(3), 263–283 (1993).
27. K. D. Paulsen and H. B. Jiang, "Enhanced frequency-domain optical image reconstruction in tissues through total-variation minimization," *Appl. Opt.* **35**(19), 3447–3458 (1996).
28. B. Kaltenbacher, A. Kirchner, and B. Vexler, "Adaptive discretizations for the choice of a Tikhonov regularization parameter in nonlinear inverse problems," *Inverse Probl.* **27**(12), 125008 (2011).
29. C. E. Chidume, C. O. Chidume, and B. Ali, "Convergence of hybrid steepest descent method for variational inequalities in Banach spaces," *Appl. Math. Comput.* **217**(23), 9499–9507 (2011).
30. Z. Strakos and P. Tichy, "On error estimation in the conjugate gradient method and why it works in finite precision computations," *Electron. Trans. Numer. Anal.* **13**, 56–80 (2002).
31. M. Rojas and T. Steihaug, "An interior-point trust-region-based method for large-scale non-negative regularization," *Inverse Probl.* **18**(5), 1291–1307 (2002).
32. J. L. Starck, E. J. Candes, and D. L. Donoho, "The curvelet transform for image denoising," *IEEE Trans. Image Process.* **11**(6), 670–684 (2002).
33. M. Elad, "Why simple shrinkage is still relevant for redundant representations," *IEEE Trans. Inform. Theor.* **52**(12), 5559–5569 (2006).
34. S. P. Zhu et al., "Cone beam micro-CT system for small animal imaging and performance evaluation," *Int. J. Biomed. Imaging* **2009**(2009), 960573 (2009).
35. G. R. Yan et al., "Fast cone-beam CT image reconstruction using GPU hardware," *J. X-Ray Sci. Technol.* **16**(4), 225–234 (2008).
36. S. A. Prahl, V. Gemert, and A. J. Welch, "Determining the optical properties of turbid media by using the adding doubling method," *Appl. Opt.* **32**(4), 559–568 (1993).
37. K. Liu et al., "Tomographic bioluminescence imaging reconstruction via a dynamically-sparse regularized global method in mouse models," *J. Biomed. Opt.* **16**(4), 046016 (2011).